Journal of the Optical Society of America A
OPTICS, IMAGE SCIENCE, AND VISION

Surface plasmon resonance sensor composed of a D-type photonic crystal fiber with a three-layer coating

Qiang Liu,[1,2] Shimiao Wang,[1,2] Haiwei Mu,[1,2] Yudan Sun,[3] Jin Zhao,[1,2] Kaiyu Wang,[1,2] Wei Liu,[1,2] Jingwei Lv,[1,2] Paul K. Chu,[4] and Chao Liu[1,2,*]

[1]SANYA Offshore Oil & Gas Research Institute, Northeast Petroleum University, Sanya 572024, China
[2]School of Physics and Electronic Engineering, Northeast Petroleum University, Daqing 163318, China
[3]College of Mechanical and Electrical Engineering, Daqing Normal University, Daqing 163712, China
[4]Department of Physics, Department of Materials Science and Engineering, and Department of Biomedical Engineering, City University of Hong Kong, Kowloon, Hong Kong, China
*msm-liu@126.com

Received 16 January 2023; revised 5 May 2023; accepted 18 May 2023; posted 19 May 2023; published 9 June 2023

A surface plasmon resonance sensor composed of photonic crystal fibers (PCF-SPR) with an Au-TiO_2-Au triple layer is designed for refractive index (RI) sensing and analyzed theoretically by the finite element method. The sensor exhibits enhanced resonance coupling between the core mode and surface plasmon polariton (SPP) mode as well as better sensitivity than the structure with a single gold coating. Furthermore, the Au-TiO_2-Au tri-layer structure narrows the linewidth of the loss spectrum and improves the figure of merit (FOM). In the analyte RI range of 1.30–1.42, the maximum wavelength sensitivity is 20,300 nm/RIU, resolution is 4.93×10^{-6}, amplitude sensitivity is 6427 RIU^{-1}, and FOM is 559 RIU^{-1}. The results provide insights into the design of high-performance PCF-SPR sensors. © 2023 Optica Publishing Group

https://doi.org/10.1364/JOSAA.485814

1. INTRODUCTION

Over the last few decades, photonic crystals have attracted extensive attention due to the existence of a bandgap and the property to limit the movement of photons. The topological edge state [1] and topological corner state [2,3] in photonic crystals provide effective ways to manipulate the propagation of light. Therefore, many novel optical devices have been discovered and investigated, such as topological photonic crystal cavities [4,5], couplers [6], sensors [7], and filters [8]. Surface plasmon resonance (SPR) sensors composed of photonic crystal fibers (PCFs) have received great interest. Compared to traditional prism-type SPR sensors [9], PCF-SPR sensors are smaller and have better electromagnetic interference resistance, corrosion resistance, and design flexibility. Moreover, PCF-SPR sensors have higher sensitivity and wider dynamic range [10,11] and have been applied to biological monitoring [12,13], food science [14], medical diagnosis [15,16], as well as environmental monitoring [17].

In order to improve the properties of PCF-SPR sensors, it is necessary to optimize the plasmonic coatings to enhance the SPR effects. Several PCF structures encompassing big air holes [18], eccentric core [19], U-type [20], D-type [21], quasi-D type [22], and lantern-type [23] have been proposed. Different materials have also been used for the outer surface of the fiber [24], inner surface of the air hole and others [25] in order to shorten the distance between the PCF fiber core mode and plasmonic coating, increase resonance coupling, and improve the refractive index (RI) sensitivity. Surface plasmonic materials are generally metals or metal oxides. In comparison with metal oxides, the SPR loss spectra of metal coatings such as palladium [26], copper (Cu) [27], silver (Ag) [28], and gold (Au) [29] typically show higher figure of merit (FOM) due to the narrow full width at half-maximum (FWHM). The average FWHM is less than 100 nm, but the wavelength sensitivity is lower [30]. Although PCF-SPR sensors based on metal oxides such as indium tin oxide (ITO) [31], zinc oxide (ZnO) [32], and titanium dioxide (TiO_2) [33] have larger peaks and higher wavelength sensitivity, the FWHM is wider and about 200–300 nm. Therefore, researchers have attempted to reduce the FWHM by using composite coatings of multiple materials to achieve higher wavelength sensitivity and FOM [34].

Shakya *et al.* have proposed an ultra-sensitive PCF-SPR biosensor based on the Au and TiO_2 bilayer coating [35] with a maximum wavelength sensitivity of 20,000 nm/RIU and FOM of 105.88 RIU^{-1}. Yang *et al*. have designed a PCF-SPR sensor with a symmetrical air hole arrangement with a TiO_2 film deposited on the Ag film [36]. This strategy solves the problem of rapid oxidation of Ag [37] and improves the

sensing characteristics at the same time. In the RI range of 1.26–1.365, the maximum FOM is 229 RIU^{-1} and the resolution is 10^{-6} [36]. Wang *et al.* have reported a Cu-ITO double-layer PCF-SPR liquid sensor [38]. In contrast to that with a single ITO layer, the FOM of the double-layer structure increases by 61.6%. In order to estimate the influence of the metal oxide, Singh *et al.* have proposed an SPR sensor based on the five-core PCF [39] and analyzed the difference between Au-ITO and Au-TiO_2. The PCF-SPR sensor composed of the Au-TiO_2 coating delivers better sensing performance and the maximum wavelength sensitivity is slightly higher than that of the Au-ITO coating. Recently, Liu *et al.* have described a $TiO_2/(SiO_2 + TiO_2)_3/Si/SiO_2/Au$ stacked structure for the prism-type SPR sensor. The Fabry–Perot resonator with the multilayer structure shows smaller FWHM and FOM increases by 5.7 times compared with the traditional SPR sensor with a single Au layer [40].

Herein, a PCF-SPR sensor with a three-layer plasmonic structure is designed. The surface of the D-type PCF is coated with Au-TiO_2-Au films to form a stacked structure. The properties of the sensor are analyzed theoretically and the difference in the performance between structures with a single Au film and Au-TiO_2-Au three-layer coating is compared. The results show that the TiO_2 dielectric waveguide layer enhances surface plasmon resonance and narrows the FWHM in the SPR loss spectra. In the RI range of 1.30–1.42, the maximum wavelength sensitivity increases from 6000 nm/RIU to 20,300 nm/RIU, the FOM increases from 96 RIU^{-1} to 559 RIU^{-1}, and the maximum amplitude sensitivity reaches 6427 RIU^{-1} for the three-layer PCF-SPR sensor.

2. DESIGN AND THEORY

A. Sensor Structure

The cross section of the D-type PCF-SPR sensor is depicted in Fig. 1(a). The PCF has a hexagonal double-layer air hole structure. The diameter of the air holes is $d = 1.2$ μm, the pitch between two adjacent air holes is $\Lambda = 2.2$ μm, the radius of the fiber is $R = 5.5$ μm, and the polished height is $h = 3.5$ μm. The Au-TiO_2-Au coating has a total thickness of $t = 60$ nm and width of $w = 7$ μm. The outer layers on the sensing structure sense the analyte and there is a perfectly matched layer. The D-type PCF can be fabricated by stacking and drawing the optical fiber preform as shown in Fig. 1(b) and then polishing the upper portion of the fiber. Another method is to stack and adjust the PCFs during the stretching process to produce the desired structure [33]. The flat surface of the D-type optical fiber is coated with Au, TiO_2, and Au sequentially by magnetron sputtering or chemical vapor deposition [41], by which the top and bottom Au films adhere strongly to the sandwiched TiO_2 layer.

The PCF-SPR sensor is made of silica and the dispersion relationship can be obtained by the Sellmeier equation [42]:

$$n(\lambda) = \sqrt{1 + \frac{0.6961663\lambda^2}{\lambda^2 - 0.0684043^2} + \frac{0.4079426\lambda^2}{\lambda^2 - 0.1162414^2} + \frac{0.8974794\lambda^2}{\lambda^2 - 9.896161^2}}, \quad (1)$$

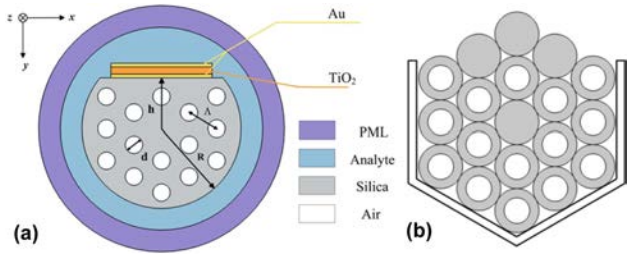

Fig. 1. (a) Cross section of the PCF-SPR sensor and (b) stacked structure of PCF.

where λ represents the wavelength of the incident light in vacuum with a unit of micrometer. The complex dielectric permittivity of gold is described by the Drude–Lorentz model [43]:

$$\varepsilon_{Au} = \varepsilon_\infty - \frac{{\omega_p}^2}{\omega^2 + i\omega\omega_\tau}, \quad (2)$$

where ε_{Au} and $\omega_p = 1.36 \times 10^{16}$ (rad/s) are the permittivity and plasmonic frequency of the gold film, respectively. The dielectric constant ε_∞ at high frequencies is 9.75, $\omega = 2\pi c/\lambda$ is the angular frequency of incident light, and $\omega_\tau = 1.45 \times 10^{14}$ (rad/s) stands for the scattering frequency of electrons. The refractive index of TiO_2 is calculated by Eq. (3) [44]:

$$n(\lambda) = \sqrt{5.913 + \frac{2.441 \times 10^7}{\lambda^2 - 0.803 \times 10^7}}. \quad (3)$$

B. Analysis of the Sensor

The properties of PCF-SPR sensors can be determined from the loss spectra of the core mode when the surface plasmonic resonance occurs. The confinement loss is defined by [45]

$$\alpha_{CL}(\text{dB/cm}) = \frac{20}{\ln(10)} \times \frac{2\pi}{\lambda} \times \text{Im}(n_{\text{eff}}) \times 10^4, \quad (4)$$

where $\text{Im}(n_{\text{eff}})$ is the imaginary part of the effective RI. When the analyte RI is $n_a = 1.39$ and the Au, TiO_2, and Au thicknesses are 15 nm/30 nm/15 nm, the loss spectra of the x-polarized and y-polarized core modes are shown in Fig. 2(a). The red solid curve and red dashed are the real parts of the effective RI of the y-polarized core mode and surface plasmon polariton (SPP) mode, respectively. The phase-matching conditions are satisfied at the intersection point. As shown by Figs. 2(b) and 2(c), the electric field distributions of the y-polarized and x-polarized core modes reveal that SPR excitation for y polarization is stronger than that of x polarization, so that the peak of the loss spectrum of the y-polarized core mode is larger than that of the x-polarized one, as manifested by the sharper and higher loss peak of the black solid curve representing y polarization compared to the blue solid curve representing x polarization in Fig. 2(a). Therefore, y polarization is chosen in the subsequent analysis.

According to the principles of the SPR sensors, the effective RI of the SPP mode changes with RIs in the vicinity. Hence, the phase-matching point is moved and the loss spectrum

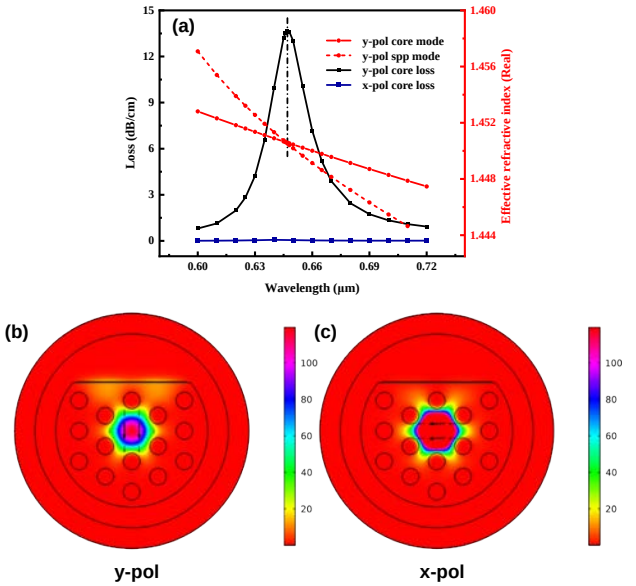

Fig. 2. Dispersion relationship of the core mode and SPP mode for the analyte RI $n_a = 1.39$: (a) confinement loss spectra, (b) electric field distribution of y polarization, and (c) electric field distribution of x polarization.

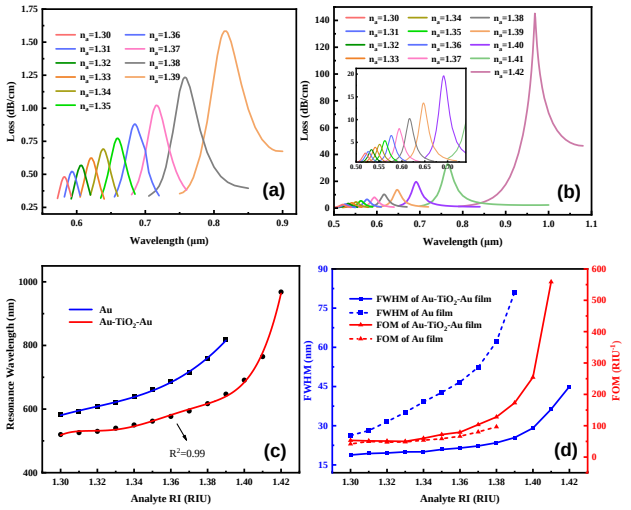

Fig. 3. Confinement loss spectra for different analyte RIs: (a) single-layer Au film and (b) three-layer Au-TiO_2-Au film; (c) resonance wavelength versus analyte RIs; and (d) FWHM and FOM curves of the single-layer and three-layer structures.

shifts. The peak wavelength of the loss spectrum is used to evaluate the wavelength sensitivity of the sensor as shown in the following [46]:

$$S_w(\text{nm/RIU}) = \frac{\Delta\lambda_p}{\Delta n_a}, \tag{5}$$

where $\Delta\lambda_p$ is the peak wavelength shift and Δn_a is the variation of the analyte RI. The wavelength resolution of the sensor can be expressed as [47]

$$R = \frac{\Delta n_a \times \Delta\lambda_{\min}}{\Delta\lambda_p}, \tag{6}$$

where R stands for the variation of RIs that can be resolved by the sensor when the minimum wavelength resolution of the demodulator is $\Delta\lambda_{\min} = 0.1$ nm. Similarly, the peak value of the loss spectrum is influenced by the analyte RI. The amplitude sensitivity is defined by the relationship between the amplitude and analyte RI as follows [48]:

$$S_a(\text{RIU}^{-1}) = -\frac{1}{\alpha_{\text{CL}}} \times \frac{\Delta\alpha_{\text{CL}}}{\Delta n_a}, \tag{7}$$

where α_{CL} is the loss at the wavelength, and $\Delta\alpha_{\text{CL}}$ is the loss difference between two adjacent RIs. The performance of the SPR sensor is assessed by the FOM defined as the quotient of the wavelength sensitivity and FWHM of the loss spectrum as follows [49]:

$$\text{FOM}(\text{RIU}^{-1}) = \frac{S_w}{\text{FWHM}}, \tag{8}$$

where FWHM represents the full width at half-maximum of the peak. Hence, the objective is to increase the wavelength sensitivity and decrease the FWHM in the loss spectrum.

In order to verify the effects of the Au-TiO_2-Au coating on the characteristics of the PCF-SPR sensor, the variation of the loss spectra of the structures with a single Au coating and Au-TiO_2-Au three-layer coating with analyte RIs are derived and compared with the same parameters. As shown in Figs. 3(a) and 3(b), when the thicknesses of the single Au film and the Au-TiO_2-Au three-layer film are 60 nm and 15 nm/30 nm/15 nm, the loss spectra show the same variation trend with increasing RIs. It is because the effective index of the SPP mode increases with increasing analyte RIs, while the effective index of the core mode remains the same, consequently producing right shifting of the phase-matching point. Therefore, the loss spectrum moves to longer wavelengths. Additionally, confinement on the core mode decreases with increasing wavelength resulting in enhanced surface plasmonic resonance effect and the loss peaks increase with RIs. The peak loss of the three-layer coating is larger than that of the single-layer Au coating. In addition, it can be seen that the refractive index ranges of the two PCF-SPR sensors are different, which is caused by the different coating materials. Figure 3(c) compares the variation of the resonant wavelengths of the two structures with analyte RIs. Although the sensitivity of the single-layer PCF-SPR sensor is slightly greater than that of the three-layer structure in the measurement range, the FWHM of the three-layer coating sensor is significantly better than that of the single-layer structure. Moreover, the FOM improves in the range of 1.35–1.41, as shown in Fig. 3(d). The maximum wavelength resolution of the sensor is 4.93×10^{-6} calculated by Eq. (6).

The amplitude sensitivity of the three-layer PCF-SPR sensor is derived by Eq. (7) as illustrated in Fig. 4. The interactions between the core mode and SPP mode become stronger as the analyte RIs increase and hence, the amplitude sensitivity increases progressively reaching a maximum of 6427 RIU^{-1} for $n_a = 1.41$.

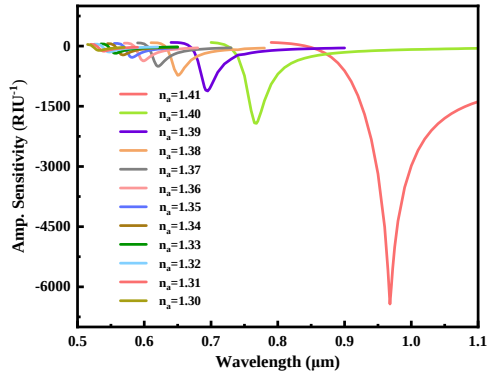

Fig. 4. Amplitude sensitivity for different RI analytes.

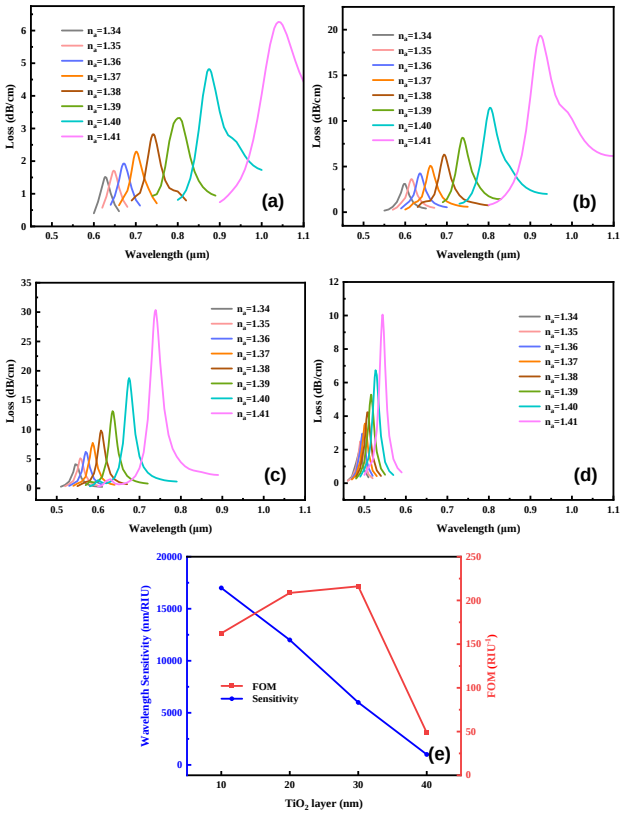

Fig. 5. Variation of PCF-SPR loss spectra with RIs for different Au-TiO_2-Au thicknesses: (a) 25 nm/10 nm/25 nm, (b) 20 nm/20 nm/20 nm, (c) 15 nm/30 nm/15 nm, and (d) 10 nm/40 nm/10 nm; (e) maximum wavelength sensitivity and FOM.

3. OPTIMIZATION AND DISCUSSION

The optimal structural parameters of the PCF-SPR sensor are $d = 1.2$ μm, $\Lambda = 2.2$ μm, $R = 5.5$ μm, $h = 3.5$ μm, and $w = 5$ μm, and the loss spectra of the sensors with different thicknesses of Au, TiO_2, and Au are presented in Figs. 5(a)–5(d). When the total thickness $t = 60$ nm of tri-layer is constant and the thickness of waveguide layer TiO_2 is increased from 10 nm to 40 nm, the whole loss spectra blueshift. Meanwhile the wavelength sensitivity and FWHM decrease simultaneously, implying that there is an optimal FOM

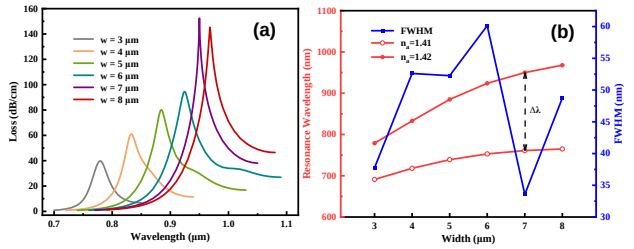

Fig. 6. (a) Loss spectra for different coating widths as $n_a = 1.42$ and (b) resonance wavelengths of the loss spectra for $n_a = 1.41-1.42$ and FWHM for $n_a = 1.42$.

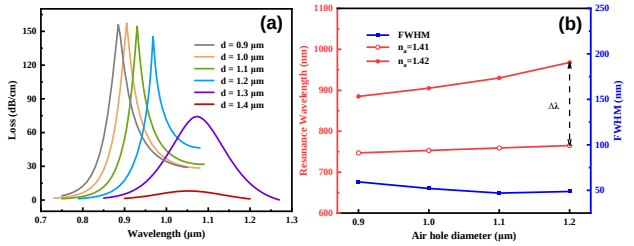

Fig. 7. (a) Loss spectra for different air hole diameters and $n_a = 1.42$ and (b) peak wavelengths of the loss spectra as n_a is changed from 1.41 to 1.42 and FWHM for $n_a = 1.42$.

according to Eq. (8). Figure 5(e) shows the maximum wavelength sensitivity and FOM in the RI range of 1.40–1.41. The wavelength sensitivity decreases with increasing TiO_2 film thickness. It is because the thicker TiO_2 film weakens the coupling between the core and the SPP mode, which negatively impacts the coupling efficiency and results in poor sensitivity. When the TiO_2 film thickness is 30 nm, the FOM reaches a maximum value of 216 RIU^{-1}. Therefore, 15 nm, 30 nm, and 15 nm are chosen as the optimal thicknesses of the three layers in the Au-TiO_2-Au structure.

When the analyte RI is 1.42, the loss spectra for different coating widths are calculated and shown in Fig. 6(a). The resonance wavelength redshifts with increasing width and the maximum loss is obtained when $w = 7$ μm. For larger widths, more energy of the core mode diffuses into the cladding and resonant coupling weakens giving rise to decreased peak loss [50]. When the analyte RI is changed from 1.41 to 1.42, the peak wavelength variation of the loss spectra for different coating widths in Fig. 6(b) shows a larger difference. It means that the wavelength sensitivity increases with increasing coating widths. At the same time, the FWHM reaches the minimum when $n_a = 1.42$ and $w = 7$ μm. Considering the overall performance of the sensor, the width of the coating is fixed at 7 μm.

Figure 7(a) shows the loss spectra for different air hole diameters for an analyte RI of 1.42. As the air hole diameter d goes up, the effective RI of the core mode decreases and the loss spectra redshift. Meanwhile, air holes with a larger diameter produce better confinement to the core mode and hinder coupling between the core mode and SPP mode. As a result, the peak loss decreases with increasing d. Figure 7(b) compares the wavelength sensitivity and FWHM for different air hole diameters. The wavelength sensitivity reaches the maximum at $d = 1.2$ μm

Table 1. Comparison of the Properties of Our Sensor and Those with Different Coatings Reported in the Literature

Refs.	Coatings	RI Range	Max Wave. Sens. (nm/RIU)	Resolution (RIU) (Wave. Int)	Max Amp. Sens. (RIU^{-1})	Max FOM (RIU^{-1})
[24]	Ag	1.33–1.37	4200	2.38×10^{-5}	300	84
[51]	Au	1.35–1.41	14500	6.9×10^{-6}	4738	387
[52]	ITO	1.22–1.33	15000	6.67×10^{-6}	442.47	75
[53]	Ag-ZnO	1.37–1.41	6000	1.67×10^{-5}	N/A	12
[54]	Au-TiO_2	1.25–1.43	6800	1.47×10^{-5}	5440	363
[55]	Au-MoS_2-gra.	1.33–1.40	14933	6.69×10^{-6}	N/A	401
This work	Au-TiO_2-Au	1.30–1.42	20300	4.93×10^{-6}	6427	559

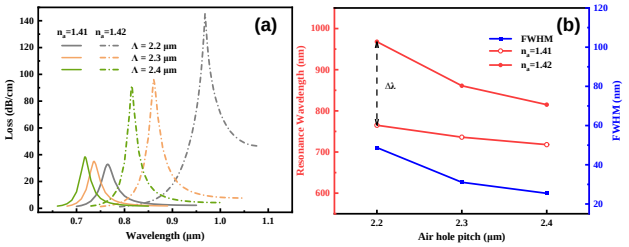

Fig. 8. (a) Loss spectra for different air hole pitches for $n_a = 1.41-1.42$ and (b) peak wavelengths of the loss spectra for $n_a = 1.41-1.42$ and FWHM for $n_a = 1.42$.

and the FWHM is relatively narrow. Therefore, $d = 1.2$ μm is selected as the optimal air hole diameter.

The loss spectra for different air hole pitches Λ are shown in Fig. 8(a) for analyte RIs of 1.41 and 1.42. Figure 8(b) shows the variations of the peak wavelength and FWHM when the air hole pitch Λ is changed from 2.2 to 2.4 μm. Although the FWHM decreases with increasing air hole pitch Λ, the maximum peak wavelength difference and FOM are 20,300 nm/RIU and 559 RIU^{-1}, respectively, at $\Lambda = 2.2$ μm. Therefore, the optimal air hole pitch is $\Lambda = 2.2$ μm.

Based on our analysis, the optimal parameters of the PCF-SPR sensor are as follows: $d = 1.2$ μm, $\Lambda = 2.2$ μm, $R = 5.5$ μm, $h = 3.5$ μm, $w = 7$ μm, $t = 15$ nm/30 nm /15 nm. In the RI range of 1.30–1.42 the maximum wavelength sensitivity is 20,300 nm/RIU, the resolution is 4.93×10^{-6}, the amplitude sensitivity is 6427 RIU^{-1}, and the maximum FOM is 559 RIU^{-1}. The properties of the sensor are compared with those of similar sensors in Table 1 confirming that the measurement accuracy and sensitivity of the three-layer structure are better than those of the double-layer and single-layer ones.

4. CONCLUSION

A three-layer stacked structure is incorporated into the D-type PCF-SPR sensor to enhance the properties. According to theoretical assessment by the finite element method, the PCF-SPR sensor has a maximum wavelength sensitivity of 20,300 nm/RIU and amplitude sensitivity of 6427 RIU^{-1} in the refractive index range of 1.30–1.42. Compared to the structure composed of a single coating, the three-layer sensor exhibits a wider detection range, improved FOM from 96 RIU^{-1} to 559 RIU^{-1}, as well as better sensing accuracy. Owing to the outstanding properties, the sensor has large prospects in sensing applications such as biomedicine and environmental monitoring.

Funding. City University of Hong Kong (7005505, DON-RMG 9229021); Natural Science Foundation of Heilongjiang Province (LH2021F007); China Postdoctoral Science Foundation (2020M670881); Northeast Petroleum University (KYCXTD201801, ts26180221); Hainan Provincial Department of Science and Technology (ZDYF2022GXJS003).

Disclosures. The authors declare no conflicts of interest.

Data availability. Data underlying the results presented in this paper are not publicly available at this time but may be obtained from the authors upon reasonable request.

REFERENCES

1. B. Yan, Y. Peng, A. Shi, J. Xie, P. Peng, and J. Liu, "Pseudo-spin-valley coupled topological states protected by different symmetries in photonic crystals," Opt. Lett. **47**, 2044–2047 (2022).
2. Q. Xu, Y. Peng, B. Yan, A. Shi, P. Peng, J. Xie, and J. Liu, "Multiband topological states in the Penrose-triangle photonic crystals," Opt. Lett. **48**, 101–104 (2023).
3. Y. Peng, E. Liu, B. Yan, J. Xie, A. Shi, P. Peng, H. Li, and J. Liu, "Higher-order topological states in two-dimensional Stampfli-Triangle photonic crystals," Opt. Lett. **47**, 3011–3014 (2022).
4. R. Ge, X. Yan, Z. Liang, H. Li, J. Wu, X. Liu, Y. Chen, and X. Chen, "Large quality factor enhancement based on cascaded uniform lithium niobate bichromatic photonic crystal cavities," Opt. Lett. **48**, 113–116 (2023).
5. P. Peng, E. Liu, B. Yan, Y. Peng, A. Shi, J. Xie, H. Li, Y. Xiang, and J. Liu, "Pair-partitioned bulk localized states induced by topological band inversion," Appl. Phys. Lett. **121**, 011103 (2022).
6. M. R. Yuan, X. Han, H. F. Xiao, T. G. Nguyen, A. Boes, G. H. Ren, Q. F. Hao, J. Z. Xue, A. Mitchell, and Y. H. Tian, "Integrated lithium niobate polarization beam splitter based on a photonic-crystal-assisted multimode interference coupler," Opt. Lett. **48**, 171–174 (2023).
7. W. Liu, Y. Shi, Z. Yi, C. Liu, F. Wang, X. Li, J. Lv, L. Yang, and P. K. Chu, "Surface plasmon resonance chemical sensor composed of a microstructured optical fiber for the detection of an ultra-wide refractive index range and gas-liquid pollutants," Opt. Express **29**, 40734–40747 (2021).
8. B. Yan, A. R. Wang, E. X. Liu, W. Tan, J. L. Xie, R. Ge, and J. J. Liu, "Polarization filtering in the visible wavelength range using surface plasmon resonance and a sunflower-type photonic quasi-crystal fiber," J. Phys. D **51**, 155105 (2018).
9. P. Zhang, L. Liu, Y. He, X. Chen, K. Ma, and D. Wei, "A waveguide-coupled surface plasmon resonance sensor using an Au-MgF_2-Au structure," Plasmonics **14**, 187–195 (2018).
10. Y. L. Deng, M. Li, W. Cao, M. Wang, H. Hao, W. Xia, and F. Su, "Fiber optic coupled surface plasmon resonance sensor based Ag-TiO_2 films for hydrogen detection," Opt. Fiber Technol. **65**, 102616 (2021).
11. T. Wang, M. J. Zhang, K. Liu, J. F. Jiang, Y. H. Zhao, J. Y. Ma, and T. G. Liu, "The effect of the TiO_2 film on the performance of the optical fiber SPR sensor," Opt. Commun. **448**, 93–97 (2019).
12. Z. Zheng, Y. Zheng, Y. Luo, Z. Yi, J. Zhang, Z. Liu, W. Yang, Y. Yu, X. Wu, and P. Wu, "A switchable terahertz device combining ultra-wideband absorption and ultra-wideband complete reflection," Phys. Chem. Chem. Phys. **24**, 2527–2533 (2022).

13. F. Zhao, J. Lin, Z. Lei, Z. Yi, F. Qin, J. Zhang, L. Liu, X. Wu, W. Yang, and P. Wu, "Realization of 18.97% theoretical efficiency of 0.9 μm thick c-Si/ZnO heterojunction ultrathin-film solar cells via surface plasmon resonance enhancement," Phys. Chem. Chem. Phys. **24**, 4871–4880 (2022).
14. L. L. S. Canabady-Rochelle, K. Selmeczi, S. Collin, A. Pasc, L. Muhr, and S. Boschi-Muller, "SPR screening of metal chelating peptides in a hydrolysate for their antioxidant properties," Food Chem. **239**, 478–485 (2018).
15. S. Jabbari, B. Dabirmanesh, S. S. Arab, M. Amanlou, S. Daneshjou, S. Gholami, and K. Khajeh, "A novel enzyme based SPR-biosensor to detect bromocriptine as an ergoline derivative drug," Sens. Actuators B **240**, 519–527 (2017).
16. D. Rajeswari and A. A. Revathi, "Highly sensitive SPR-based PCF bio sensor for plasma cell detection in human blood for the detection of early stage cancer," Optik **258**, 168897 (2022).
17. L. S. Goh, N. Kumekawa, K. Watanabe, and N. Shinomiya, "Hetero-core spliced optical fiber SPR sensor system for soil gravity water monitoring in agricultural environments," Comput. Electron. Agric. **101**, 110–117 (2014).
18. M. S. Islam, J. Sultana, A. A. Rifat, R. Ahmed, A. Dinovitser, B. W. Ng, H. Ebendorff-Heidepriem, and D. Abbott, "Dual-polarized highly sensitive plasmonic sensor in the visible to near-IR spectrum," Opt. Express **26**, 30347–30361 (2018).
19. M. Biplob Hossain, S. M. Riazul Islam, K. M. Tasrif Hossain, L. Faisal Abdulrazak, M. Nazmus Sakib, and I. S. Amiri, "High sensitivity hollow core circular shaped PCF surface plasmonic biosensor employing silver coat: a numerical design and analysis with external sensing approach," Results Phys. **16**, 102909 (2020).
20. Q. Liu, Y. Jiang, Y. Sun, C. Hu, J. Sun, C. Liu, J. Lv, J. Zhao, Z. Yi, and P. K. Chu, "Surface plasmon resonance sensor based on U-shaped photonic quasi-crystal fiber," Appl. Opt. **60**, 1761–1766 (2021).
21. C. Li, B. Yan, and J. Liu, "Refractive index sensing characteristics in a D-shaped photonic quasi-crystal fiber sensor based on surface plasmon resonance," J. Opt. Soc. Am. A **36**, 1663–1668 (2019).
22. T. Huang, "Highly sensitive SPR sensor based on D-shaped photonic crystal fiber coated with indium tin oxide at near-infrared wavelength," Plasmonics **12**, 583–588 (2016).
23. Q. Liu, J. Zhao, Y. Sun, W. Liu, C. Liu, J. Lv, T. Lv, Y. Jiang, B. Li, F. Wang, T. Sun, and P. K. Chu, "High-sensitivity methane sensor composed of photonic quasi-crystal fiber based on surface plasmon resonance," J. Opt. Soc. Am. A **38**, 1438–1442 (2021).
24. M. R. Momota and M. R. Hasan, "Hollow-core silver coated photonic crystal fiber plasmonic sensor," Opt. Mater. **76**, 287–294 (2018).
25. S. H. Zhang, J. S. Li, S. G. Li, Q. Liu, J. J. Wu, and Y. Guo, "Surface plasmon resonance sensor based on D-shaped photonic crystal fiber with two micro-openings," J. Phys. D **51**, 305104 (2018).
26. Y. N. Zhang, H. J. Peng, X. L. Qian, Y. Y. Zhang, G. W. An, and Y. Zhao, "Recent advancements in optical fiber hydrogen sensors," Sens. Actuators B **244**, 393–416 (2017).
27. V. Kapoor, N. K. Sharma, S. Gupta, and P. Kumar, "Fiber optic SPR sensing of liquids using copper and zinc oxide," Optik **238**, 166727 (2021).
28. N. A. M. Zainuddin, M. M. Ariannejad, P. T. Arasu, S. W. Harun, and R. Zakaria, "Investigation of cladding thicknesses on silver SPR based side-polished optical fiber refractive-index sensor," Results Phys. **13**, 102255 (2019).
29. W. Liu, C. Liu, J. Wang, J. Lv, Y. Lv, L. Yang, N. An, Z. Yi, Q. Liu, C. Hu, and P. K. Chu, "Surface plasmon resonance sensor composed of microstructured optical fibers for monitoring of external and internal environments in biological and environmental sensing," Results Phys. **47**, 106365 (2023).
30. V. K. Walia and R. K. Verma, "Lossy mode resonance-based uniform core tapered fiber optic sensor for sensitivity enhancement," Commun. Theor. Phys. **72**, 095502 (2020).
31. Q. Liu, J. D. Sun, Y. D. Sun, Z. H. Ren, C. Liu, J. W. Lv, F. M. Wang, L. Y. Wang, W. Liu, T. Sun, and P. K. Chu, "Surface plasmon resonance sensor based on photonic crystal fiber with indium tin oxide film," Opt. Mater. **102**, 109800 (2020).
32. V. Kaur and S. Singh, "Design of D-shaped PCF-SPR sensor with dual coating of ITO and ZnO conducting metal oxide," Optik **220**, 165135 (2020).
33. A. A. Rifat, R. Ahmed, G. A. Mahdiraji, and F. R. M. Adikan, "Highly sensitive D-shaped photonic crystal fiber-based plasmonic biosensor in visible to near-IR," IEEE Sens. J. **17**, 2776–2783 (2017).
34. M. R. Islam, M. M. I. Khan, S. Siraz, F. Mehjabin, M. Rahman, M. Islam, M. S. Anzum, J. A. Chowdhury, and F. Noor, "Design and analysis of a QC-SPR-PCF sensor for multipurpose sensing with supremely high FOM," Appl. Nanosci. **12**, 29–45 (2022).
35. A. K. Shakya, A. Ramola, S. Singh, and V. Van, "Design of an ultra-sensitive bimetallic anisotropic PCF SPR biosensor for liquid analytes sensing," Opt. Express **30**, 9233–9255 (2022).
36. H. M. Yang, G. Y. Wang, Y. Lu, and J. Q. Yao, "Highly sensitive refractive index sensor based on SPR with silver and titanium dioxide coating," Opt. Quantum Electron. **53**, 341 (2021).
37. S. Singh and Y. K. Prajapati, "TiO_2/gold-graphene hybrid solid core SPR based PCF RI sensor for sensitivity enhancement," Optik **224**, 165525 (2020).
38. Q. Wang, B. Sun, E. T. Hu, and W. Wei, "Cu/ITO-coated uncladded fiber-optic biosensor based on surface plasmon resonance," IEEE Photonics Technol. Lett. **31**, 1159–1162 (2019).
39. A. K. Shakya and S. Singh, "Design of refractive index sensing based on optimum combination of plasmonic materials gold with indium tin oxide/titanium dioxide," J. Nanophotonics **16**, 026010 (2022).
40. G. S. Liu, X. Xiong, S. Q. Hu, W. C. Shi, Y. F. Chen, W. G. Zhu, H. D. Zheng, J. H. Yu, N. H. Azeman, Y. H. Luo, and Z. Chen, "Photonic cavity enhanced high-performance surface plasmon resonance biosensor," Photonics Res. **8**, 448–456 (2020).
41. S. Das, S. Guha, P. P. Das, and R. K. Ghadai, "Analysis of morphological, microstructural, electrochemical and nano mechanical characteristics of TiCN coatings prepared under N_2 gas flow rate by chemical vapour deposition (CVD) process at higher temperature," Ceram. Int. **46**, 10292–10298 (2020).
42. G. Ghosh, M. Endo, and T. Iwasaki, "Temperature-dependent Sellmeier coefficients and chromatic dispersions for some optical fiber glasses," J. Lightwave Technol. **12**, 1338–1342 (1994).
43. A. Vial, A.-S. Grimault, D. Macías, D. Barchiesi, and M. L. de la Chapelle, "Improved analytical fit of gold dispersion: application to the modeling of extinction spectra with a finite-difference time-domain method," Phys. Rev. B **71**, 085416 (2005).
44. J. R. DeVore, "Refractive indices of rutile and sphalerite," J. Opt. Soc. Am. A **41**, 416–419 (1951).
45. E. X. Liu, S. W. Liang, and J. J. Liu, "Double-cladding structure dependence of guiding characteristics in six-fold symmetric photonic quasi-crystal fiber," Superlattices Microstruct. **130**, 61–67 (2019).
46. C. Liu, L. Yang, Q. Liu, F. Wang, Z. Sun, T. Sun, H. Mu, and P. K. Chu, "Analysis of a surface plasmon resonance probe based on photonic crystal fibers for low refractive index detection," Plasmonics **13**, 779–784 (2017).
47. M. Hautakorpi, M. Mattinen, and H. Ludvigsen, "Surface-plasmon-resonance sensor based on three-hole microstructured optical fiber," Opt. Express **16**, 8427–8432 (2008).
48. B. Gauvreau, A. Hassani, M. Fassi Fehri, A. Kabashin, and M. A. Skorobogatiy, "Photonic bandgap fiber-based surface plasmon resonance sensors," Opt. Express **15**, 11413–11426 (2007).
49. C. Liu, W. Su, Q. Liu, X. Lu, F. Wang, T. Sun, and P. K. Chu, "Symmetrical dual D-shape photonic crystal fibers for surface plasmon resonance sensing," Opt. Express **26**, 9039–9049 (2018).
50. W. Y. Zeng, Q. L. Wang, and L. Xu, "Plasmonic refractive index sensor based on D-shaped photonic crystal fiber for wider range of refractive index detection," Optik **223**, 165463 (2020).
51. M. R. Islam, A. N. M. Iftekher, K. R. Hasan, M. J. Nayen, S. Bin Islam, R. Islam, R. L. Khan, E. Moazzam, and Z. Tasnim, "Surface plasmon resonance based highly sensitive gold coated PCF biosensor," Appl. Phys. A **127**, 118 (2021).
52. C. Liu, J. W. Wang, F. M. Wang, W. Q. Su, L. Yang, J. W. Lv, G. L. Fu, X. L. Li, Q. Liu, T. Sun, and P. K. Chu, "Surface plasmon resonance (SPR) infrared sensor based on D-shape photonic crystal fibers with ITO coatings," Opt. Commun. **464**, 125496 (2020).
53. H. Liang, T. Shen, Y. Feng, H. Liu, and W. Han, "A D-shaped photonic crystal fiber refractive index sensor coated with graphene and zinc oxide," Sensors **21**, 71 (2020).

54. H. R. Wang, W. Y. Rao, J. Luo, and H. Y. Fu, "A dual-channel surface plasmon resonance sensor based on dual-polarized photonic crystal fiber for ultra-wide range and high sensitivity of refractive index detection," IEEE Photonics J. **13**, 6800611 (2021).

55. S. Singh and Y. K. Prajapati, "Dual-polarized ultrahigh sensitive gold/MoS_2/graphene based D-shaped PCF refractive index sensor in visible to near-IR region," Opt. Quantum Electron. **52**, 17 (2019).

144.214.9.191 {ts '2023-06-09 20:37:29'}